Journal of
Marine Science and Engineering

MDPI

Article

An Experimental Study of Three-Dimensional Separation Surface Sloshing in the Wet Storage Tank of a Floating Offshore Platform

Dongxi Liu [1], Xiaoying Wang [1] and Yujiao Chen [2,*]

[1] College of Ocean Science and Engineering, Shanghai Maritime University, Shanghai 201306, China; dxliu@shmtu.edu.cn (D.L.)
[2] College of Information Technology, Shanghai Jian Qiao University, Shanghai 201306, China
* Correspondence: chenyujiao@gench.edu.cn

Abstract: In this work, in order to elucidate the three-dimensional (3D) resonant sloshing dynamics of the oil–water interface in an offshore cylindrical wet storage tank, a series of model experiments are conducted in a completely filled cylindrical tank containing two immiscible liquids. To begin with, a series of free damping tests are performed to experimentally determine the viscous damping rate of the system and to examine the corresponding theoretical solutions. Subsequently, the separation surface wave responses at a series of excitation frequencies including the natural frequencies of first five modes are examined. Finally, the rotary sloshing dynamics at the natural frequencies of the first and second natural modes are systematically explored. Interestingly, it is found that the separation surface rotary sloshing in a two-layer liquid system is much more intricate than one-layer liquid rotary sloshing due to the generation of multitudinous short waves in the long wave. As far as we know, this is the first investigation of 3D separation surface rotary wave motion in a two-layer liquid system without a free surface.

Keywords: cylindrical tank; two-layer liquid; separation surface sloshing; wave rotation; viscous damping; long–short wave

check for updates

Citation: Liu, D.; Wang, X.; Chen, Y. An Experimental Study of Three-Dimensional Separation Surface Sloshing in the Wet Storage Tank of a Floating Offshore Platform. *J. Mar. Sci. Eng.* **2024**, *12*, 558. https://doi.org/10.3390/jmse12040558

Academic Editor: José António Correia

Received: 2 March 2024
Revised: 20 March 2024
Accepted: 25 March 2024
Published: 27 March 2024

Copyright: © 2024 by the authors. Licensee MDPI, Basel, Switzerland. This article is an open access article distributed under the terms and conditions of the Creative Commons Attribution (CC BY) license (https://creativecommons.org/licenses/by/4.0/).

1. Introduction

In recent decades, many large oil and gas fields have been discovered in the deep waters of Brazil, West Africa, the Gulf of Mexico, and other "hot" frontier areas. The huge costs of the exploitation of these deep-water oil and gas fields using traditional methods provide an incentive to look for new development programs. One method being promoted by several oil companies is the use of floating multifunction platforms, which integrate the functions of a drilling platform and floating production, storage, and offloading (FPSO). These floating, drilling, production, storage, and offloading (FDPSO) platforms not only reduce the overall facility costs but also accelerate the speed of field development [1,2].

Two different techniques are used to store crude oil [3]. One approach is "dry" storage, in which the oil is stored in a dry tank. This approach is typically employed in FPSO and ship-shaped FDPSO but is not applicable to cylinder-shaped FDPSO since the oil storage tanks also serve as ballast tanks for the platform. The other approach is "wet" storage, which involves the storage of oil with seawater by using the oil/water displacement principle. Because of the density difference between seawater and crude oil, the crude oil occupies the upper space in the storage tanks, whereas the seawater remains in the lower space. Initially, the storage tanks are full of seawater. During production, the produced crude oil displaces the same volume of seawater out to sea through a sewage disposal system, while during offloading, the exported crude oil is displaced by the seawater that directly enters the bottom of the tanks. In other words, the tanks are always completely filled with either seawater or crude oil. This approach, which is also widely employed

for subsea oil storage tanks [4] and gravity-based structures [5], allows for better control over the stability of the floating platform by incorporating the oil storage operation into its ballasting procedure.

In a marine environment, the sloshing of the oil–water separation surface in wet storage tanks is probably triggered due to the wave-induced motion of the floating platforms, and this promotes the emulsification of the oil and water and accelerates the heat transfer between the oil and water. Consequently, separation surface sloshing adversely affects the economy of FDPSO, and it must be considered when designing wet storage tanks. Meanwhile, it is worth pointing out that separation surface sloshing not only takes place in wet storage tanks but also in three-phase separators installed on the decks of various floating production platforms. Besides the marine industry, separation surface sloshing dynamics also occur in other engineering fields, such as civil, mechanical, and new energy industries [6–8].

The sloshing of the free liquid surface has motivated an enormous number of theoretical, experimental, and numerical studies [9–12]. A summary of the relevant investigations performed in the past few decades is available in Ibrahim [13], Faltinsen and Timokha [6], Ibrahim [7], and Igbadumhe and Furth [14]. However, not much work has been conducted to explore separation surface sloshing in tanks with two or more immiscible liquids. Intensive experimental studies on two-layer liquid sloshing were performed by Liu et al. [15] and Liu and Li [16]; they found that the sloshing dynamics of the separation surface between two liquids are much more intricate than that of the free surface. Beyond experimental approaches, theoretical and numerical models can be employed to investigate separation surface sloshing. For example, Xue et al. [17] conducted a semi-analytic study of the suppression effect of a horizontal baffle on two-layer liquid sloshing, and the results demonstrated that the density difference became more important for the coupled frequency when the baffle was in the upper-layer liquid. Cao et al. [18] used the volume-of-fluid (VOF) method to explore the free surface and separation surface sloshing dynamics in a rectangular tank under horizontal excitation. It was observed that the sloshing responses of the free surface and the separation interface could be in-phase or completely different. For example, it could be that the wave profile at the free surface is a standing wave, while that at the separation interface is a traveling wave. In order to verify the active control concept, which can mitigate the sloshing of the oil surface and the oil–water interface in horizontal three-phase separators on floating production facilities, a series of VOF simulation works were conducted by Frankiewicz and Lee [19], Lu and Chai [20], and Cen et al. [21]. These investigations confirmed that the sloshing response is closely related to factors including the length-to-diameter ratio, the configuration of the baffles, and the incident direction of the wave. Luo et al. [22] used the consistent particle method (CPM) to study the two-layer liquid sloshing in a rectangular tank under sway or coupled sway–heave excitations. However, the generation and growth of shorter waves at the separation interface cannot be accurately described using these mesh-based or meshless numerical methods.

In order to elucidate the resonant separation surface sloshing dynamics in a laterally excited cylindrical tank, extensive experiments are conducted in a completely filled model tank with two fluids—dyed water and mineral oil. This paper is organized as follows. Section 2 presents the composition of the experimental setup and also describes the theoretical background for the present separation surface sloshing problem, including the natural frequencies and corresponding natural modes, the linear solution for the separation surface wave elevation, the prediction of the viscous damping rate, and the choice of a non-dimensional number. In Section 3, the viscous damping rate and the sloshing natural frequency obtained using linear theory are verified using free damping tests. Subsequently, the separation surface wave responses at a series of excitation frequencies including the first five modes of natural frequencies are examined in Section 4. In Sections 5 and 6, 3D separation surface sloshing dynamics at the natural frequencies of the first and second modes are systematically investigated. Finally, conclusions are drawn in Section 7.

2. Experimental Setup and Theoretical Background

The sloshing experiments were carried out in a closed circular cylindrical tank with a diameter $D = 2R = 480$ mm and a height $H = 480$ mm, as shown in Figure 1. The tank was filled with colored water and transparent mineral oil. The depth of the water h_1 is equal to that of the oil h_2, $h_1 = h_2 = 240$ mm. The density ρ, kinematic viscosity ν, and surface tension γ of the water and oil were as follows: $\rho_1 = 998.2$ kg/m^3, $\nu_1 = 1.0 \times 10^{-6}$ m^2/s, $\gamma_1 = 0.073$ N/m, $\rho_2 = 811.5$ kg/m^3, $\nu_2 = 2.0 \times 10^{-6}$ m^2/s, and $\gamma_2 = 0.031$ N/m. Under the condition $\rho_1 > \rho_2$, two fluids stably stratify because of gravity and form a stable liquid–liquid interface. The origin of the cylindrical coordinate system $O(r, \theta, z)$ was situated in the center of the liquid–liquid interface. The liquid tank was fastened on a shake table, which was driven using an electric cylinder and equipped with a laser displacement sensor.

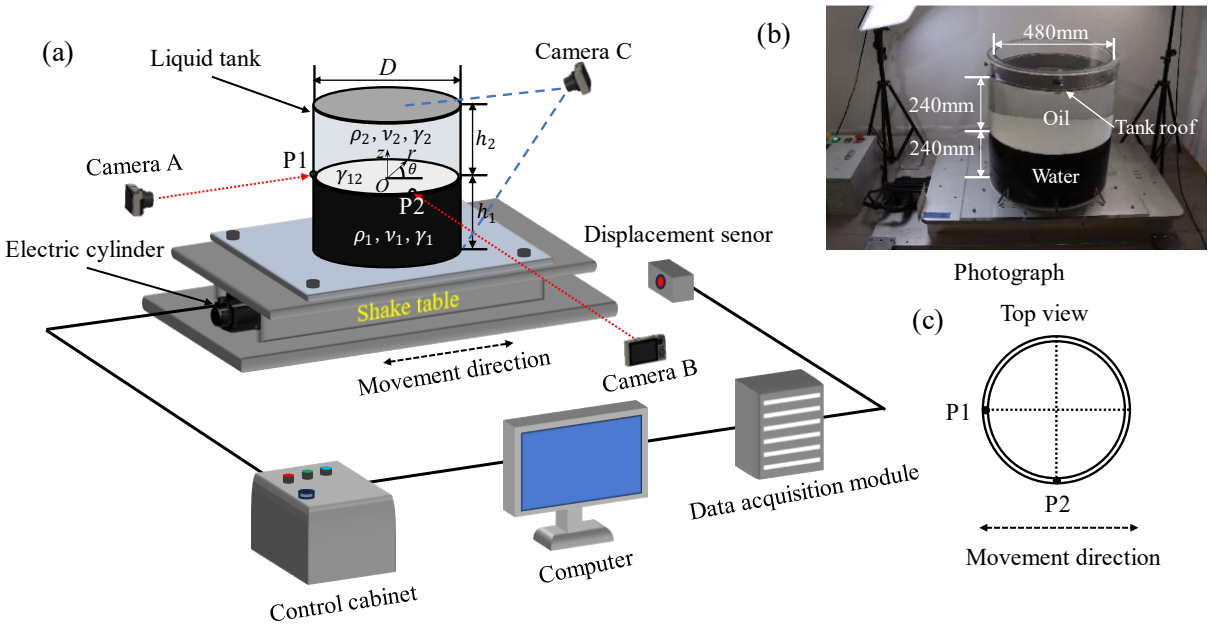

Figure 1. The experimental facility. (**a**) schematic diagram; (**b**) photograph; (**c**) location of the measurement point. The cylindrical tank ($D = 480$ mm, $H = 480$ mm) is filled with oil and water ($i = 1, 2$) of ρ_i, ν_i, γ_i, and h_i, which stably stratify because of gravity g and form a distinct oil–water interface with separation surface tension γ_{12}. The shake table induces harmonic lateral motions of amplitude A and frequency ω_e in the tank. Three high-speed charge-coupled device (CCD) cameras are installed on the tripods, which stand on the floor around the tank.

The design of the experimental cases requires us to determine the natural frequencies and corresponding natural modes accurately. Natural modes are nontrivial solutions to the linear boundary value problem for a liquid tank without external excitation. According to Faltinsen and Timokha [6] and Horstmann et al. [23], the velocity potential of the separation surface motion in a vertical cylindrical tank can be described in a cylindrical coordinate system (r, θ, z) as

$$\varphi_{mn}(r,\theta,z) = J_m(k_{mn}r)\frac{\cosh[k_{mn}(z+h_1)]}{\cosh(k_{mn}h_1)}\begin{cases} cos(m\theta) \\ sin(m\theta) \end{cases} \quad (1)$$

The separation surface wave forms of the natural modes are defined as

$$\psi_{mn}(r,\theta) = \varphi_{mn}(r,\theta,0) = J_m(k_{mn}r)\begin{cases} cos(m\theta) \\ sin(m\theta) \end{cases} \quad (2)$$

where J_m denotes the m-th order Bessel function of the first kind and h is the liquid depth. Complementarily, $k_{mn} = \lambda_{mn}/R$, where λ_{mn} are the radial wave numbers $\lambda_{11} = 1.841$, $\lambda_{12} = 5.331$, $\lambda_{13} = 8.536$, $\lambda_{14} = 11.706$, and $\lambda_{15} = 14.864$.

Depending on the force exerted on the tank, different natural modes are triggered, e.g., vertical movement is likely to generate $m = 0$ modes, while horizontal or pitching oscillation is expected to excite $m = 1$ modes. Consequently, only the $m = 1$ modes are considered in this study due to the fact that the direction of movement of the shake table is horizontal. Two-dimensional visualizations of the first three separation surface wave modes for $m = 1$ from Equation (2) are shown in Figure 2.

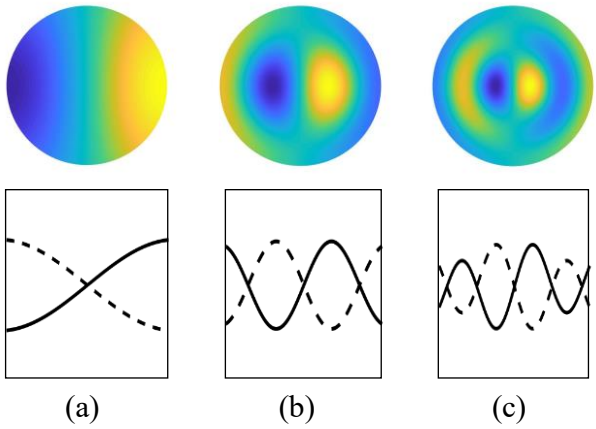

Figure 2. The wave forms associated with the first three natural modes of $m = 1$: (**a**) mode (1, 1), (**b**) mode (1, 2), (**c**) mode (1, 3).

The corresponding natural frequencies of the movement of the interface for $m = 1$ in the closed cylindrical tank filled with two immiscible liquids can be expressed as [23]

$$\omega_{1n}^2 = \frac{(\rho_1 - \rho_2)g\frac{\lambda_{1n}}{R} + \gamma_{12}\left(\frac{\lambda_{1n}}{R}\right)^3}{\rho_1 \coth\left(\frac{\lambda_{1n}}{R}h_1\right) + \rho_2 \coth\left(\frac{\lambda_{1n}}{R}h_2\right)} \tag{3}$$

The separation surface tension between the two liquids can be estimated by combining the surface tensions of the two liquids as

$$\gamma_{12} = \gamma_1 + \gamma_2 - 2\sqrt{\gamma_1\gamma_2} \tag{4}$$

It can be clearly seen that that the natural frequencies mainly depend on the density difference $\rho_1 - \rho_2$ and the ratios h_1/R and h_2/R. If $\rho_2 \to 0$, the natural frequencies for the free surface sloshing in a cylindrical tank are obtained as follows:

$$\omega_{1n}^2 = \left[\frac{g\lambda_{1n}}{R} + \frac{\gamma\lambda_{1n}^3}{\rho R^3}\right]\tanh\left(\frac{\lambda_{1n}h}{R}\right) \tag{5}$$

According to Horstmann et al. [23], the linear solution for the separation surface wave elevation η can be expressed in the following form:

$$\eta(r,\theta,t) = \sum_{n=1}^{\infty} \frac{(\rho_1-\rho_2)AR\omega_e^2}{\left[2(\rho_1-\rho_2)g + 2\left(\frac{\lambda_{1n}}{R}\right)^2\gamma_{12}\right]} \frac{J_1\left(\lambda_{1n}\frac{r}{R}\right)}{(\lambda_{1n}^2-1)J_1(\lambda_{1n})} \left[\frac{\omega_{1n}^2(\omega_{1n}^2-\omega_e^2)}{(\omega_{1n}^2-\omega_e^2)^2 + 4\delta_{1n}^2\omega_e^2}\cos(\omega_e t-\theta)\right] \tag{6}$$

If $\rho_2 \to 0$, and $\gamma_{12} \to 0$, this theoretical solution is equivalent to the theory for the elevation of the free liquid surface in a cylindrical tank with a one-layer liquid [24].

The viscous damping rate δ_{1n} is an important sloshing parameter. Here, it is determined according to theoretical prediction and an experimental measurement for our two-layer liquid system. According to Horstmann et al. [24], the viscous damping rate δ_{1n} is composed of three different contributions:

$$\delta_{1n} = \delta_{1n}^{BL} + \delta_{1n}^{IL} + \delta_{1n}^{Int} \tag{7}$$

$$\delta_{1n}^{BL} = \sum_{i=1,2} \rho_i \sqrt{\frac{\nu_i \omega_e}{8R^2}} \left[\frac{\lambda_{1n}\left(1 - \frac{h_i}{R}\right)\sinh^{-2}\left(\frac{\lambda_{1n}}{R}h_i\right) + \left(\frac{\lambda_{1n}^2+1}{\lambda_{1n}^2-1}\right)\coth\left(\frac{\lambda_{1n}}{R}h_i\right)}{\rho_1 \coth\left(\frac{\lambda_{1n}}{R}h_1\right) + \rho_2 \coth\left(\frac{\lambda_{1n}}{R}h_2\right)} \right] \tag{8}$$

$$\delta_{1n}^{IL} = \frac{\lambda_{1n}}{\left(\frac{1}{\rho_1}\sqrt{\frac{8R^2}{\omega_e \nu_1}} + \frac{1}{\rho_2}\sqrt{\frac{8R^2}{\omega_e \nu_2}}\right)} \left[\frac{\left(\coth\left(\frac{\lambda_{1n}}{R}h_1\right) + \coth\left(\frac{\lambda_{1n}}{R}h_2\right)\right)^2}{\rho_1 \coth\left(\frac{\lambda_{1n}}{R}h_1\right) + \rho_2 \coth\left(\frac{\lambda_{1n}}{R}h_2\right)} \right] \tag{9}$$

$$\delta_{1n}^{Int} = \frac{2\lambda_{1n}^2\left(\frac{\rho_2 \nu_2}{R^2} - \frac{\rho_1 \nu_1}{R^2}\right)}{\left(\frac{1}{\rho_1\sqrt{\nu_1}} + \frac{1}{\rho_2\sqrt{\nu_2}}\right)} \left[\frac{\frac{1}{\rho_1\sqrt{\nu_1}}\coth\left(\frac{\lambda_{1n}}{R}h_2\right) - \frac{1}{\rho_2\sqrt{\nu_2}}\coth\left(\frac{\lambda_{1n}}{R}h_1\right)}{\left(\rho_1 \coth\left(\frac{\lambda_{1n}}{R}h_1\right) + \rho_2 \coth\left(\frac{\lambda_{1n}}{R}h_2\right)\right)} \right] \tag{10}$$

The first contribution δ_{1n}^{BL} expresses the viscous dissipation arising at the wall boundary layers, including the top, bottom, and surrounding walls. The second contribution δ_{1n}^{IL} describes the dissipation rate in the separation surface boundary layers. The third contribution δ_{1n}^{Int} is the interior damping rate, which can be destabilizing.

We use the frequency f_n to mark the angular frequency ω_{1n}, i.e., $f_n = \omega_{1n}/2\pi$. As a consequence, for the present two-layer liquid system, the natural frequencies of the first five sloshing modes are f_1 = 0.434 Hz, f_2 = 0.759 Hz, f_3 = 0.960 Hz, f_4 = 1.124 Hz, and f_5 = 1.267 Hz.

In all the experiments, the tank was driven using horizontal harmonic motion:

$$x = A\sin(2\pi f_e t) \tag{11}$$

In order to reduce the disturbance of the interface caused by the sudden movement of the tank, a ramp function was imposed onto the driving signal during the first few periods:

$$x = A(t)\sin(2\pi f_e t) \tag{12}$$

$$A(t) = \begin{cases} A(t/T_r) & if\ 0 < t < T_r \\ A & if\ t \geq T_r \end{cases} \quad (T_r = 20\text{s}) \tag{13}$$

In this study, hundreds of experimental cases including a series of excitation frequencies f_e and excitation amplitudes A were conducted. In particular, twenty non-dimensional excitation amplitudes, i.e., A/D = 0.005−0.1, with a small increment of 0.005, were tested to examine the influence of the excitation amplitude on the separation surface sloshing dynamic. Meanwhile, dozens of non-dimensional excitation frequencies f_e/f_1, ranging from 0.5 to 3.0 and including the natural frequencies of modes (1, 1), (1, 2), (1, 3), (1, 4), and (1, 5), were employed to discuss the effect of the excitation frequency on the separation surface sloshing dynamic. In other words, the ranges of the excitation parameters employed were $2.4 \leq A \leq 48$ mm and $0.217 \leq f_e \leq 1.302$ Hz.

Concisely, the sloshing problem is governed by a series of key non-dimensional parameters. When conducting sloshing model experiments, it is essential to choose an appropriate non-dimensional number to represent the association between the sloshing dynamics in a model tank and the practical phenomenon in a full-scale tank. Following the theory for free surface sloshing in a cylindrical tank presented by Reclari et al. [25] and

the theory for separation surface sloshing in a cylindrical tank presented by Horstmann et al. [23], we chose the following five non-dimensional numbers:

$$Fr = \frac{A\omega_e^2}{g}, Re_i = \frac{\omega_e R^2}{\nu_i}, H_i = \frac{h_i}{R}, Bo = \frac{(\rho_1 - \rho_2)gR^2}{\gamma_{12}}, At = \frac{\rho_1 - \rho_2}{\rho_1 + \rho_2} \quad (14)$$

Here, the Froude number Fr represents the relation between the inertial force of the sloshing flow and the gravitational force. H_i denotes the non-dimensional aspect ratios. The Reynolds number Re_i can be used to weight the tank radius with the boundary layer thickness $\tau_i = \sqrt{\nu_i/\omega_e}$. The Bond number Bo specifies the importance of the gravitational force compared to the separation surface tension. The Atwood number At describes the transition from separation surface sloshing (small At) to free surface sloshing ($At \approx 1$).

All the relevant physical parameters of the two liquids and the corresponding non-dimensional numbers are presented in Tables 1 and 2, respectively.

Table 1. The default parameters and physical properties of the oil–water separation surface sloshing experiments.

Property	ρ (kg/m^3)	ν (m^2/s)	γ (N/m)	h (m)	R (m)
Lower layer	811.5	2.0×10^{-6}	0.031	0.24	0.24
Upper layer	998.2	1.0×10^{-6}	0.073	0.24	0.24

Table 2. The non-dimensional numbers of the oil–water separation surface sloshing experiments.

Number	Fr	Re_i	H_i	Bo	At
Lower layer	0.0005−0.33	78,000−470,000	1	11,463	0.1
Upper layer	0.0005−0.33	39,000−230,000	1	11,463	0.1

There is no doubt that the most important parameter in this experimental work is the elevation of the separation surface wave. In this work, the 3D separation surface wave motion was tracked using CCD cameras combined with rulers. As shown in Figure 1, three cameras were fixed on tripods positioned around the tank. The elevations of the separation surface wave at positions P1 and P2 were recorded using Cameras A and B, respectively. The patterns of the separation surface wave were captured using Camera C in front of the tank. Two rulers were affixed onto the external wall of the tank. The time history of the wave elevation at two measurement points can be determined using a series of still pictures extracted from the videos.

3. Determination of the Damping Rate and Natural Frequency

In 2D free surface and separation surface sloshing experiments conducted in a rectangular tank, the value of the viscous damping rate δ is constant and can be easily determined using the free damping test [26]. The damping rate of the free surface motion during the process of free damping can be calculated as $\delta = \Delta/t$, where Δ is the logarithmic decrement and t is the decay time. Δ is expressed as $\Delta = \ln(\xi_1/\xi_k)$, where ξ_1 is the wave amplitude of the first free damping cycle, ξ_k is the wave amplitude of the subsequent free damping n cycle, and k is the number of the free damping cycle. Such an approach was employed in the 2D free surface sloshing experiments of Simonini et al. [27] and Bäuerlein and Avila [28] and in the 2D separation surface sloshing experiments of Liu et al. [11,12], in which they demonstrated that the decay of the transient planar wave has an exponential form $\xi = \xi_1 e^{(-\delta t)}$. However, in 3D free surface or separation surface rotary sloshing experiments, the calculation of the viscous damping rate δ is intricate and requires careful consideration.

In order to accurately evaluate the damping rate of the present two-layer liquid system without a free surface, the free damping tests were conducted several times at different

initial oscillation amplitudes. Figure 3 shows the time series of the separation surface displacement η at (i) P1 and (ii) P2 during free damping for four decay experiments, called Case A (f_e/f_1 = 1.0, A/D = 0.025), Case B (f_e/f_1 = 1.0, A/D = 0.05), Case C (f_e/f_1 = 1.0, A/D = 0.075), and Case D (f_e/f_1 = 1.0, A/D = 0.1). The time t is normalized to the excitation period T_e, where $T_e = 1/f_e$.

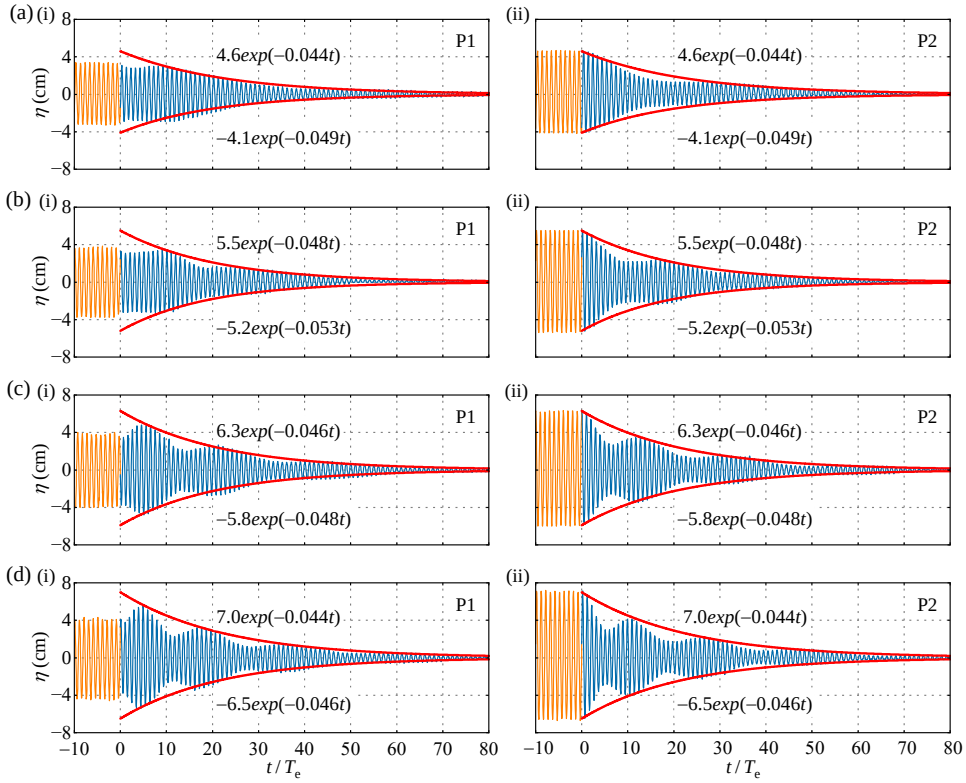

Figure 3. The decay of the separation surface displacement η of the primary natural mode of the system, measured at (**i**) P1 and (**ii**) P2 for decay experiments: (**a**) Case A, (**b**) Case B, (**c**) Case C, and (**d**) Case D. At t = 0, the external excitation was turned off to measure the damping rate. The motions of the separation surface wave during both the steady state ($t \leq 0$) and the decaying state ($t > 0$) are the 3D rotary wave.

In all instances, it can be observed that the movement of the separation surface is a rotary wave with a constant amplitude before the cessation of the tank's movement. However, it fades into a rotary wave with a decreasing amplitude after stopping the driving. As shown in Figure 3a(ii), during the first 15 periods following the cessation of the tank's movement, the decay of the amplitude of the transient rotary wave occurred much faster than in the subsequent dozens of periods. This is because of the nonlinear energy transfer between the points parallel (P1) and perpendicular (P2) to the tank's movement direction that occurs when the rotary wave amplitude is large [see Figure 3a(i)]. With an increase in the initial oscillation amplitude, a beating behavior occurs at both P1 and P2. Similarly to the case of a 2D planar wave, the damping rate of a 3D rotary wave is determined by fitting the exponential formula $\xi = \xi_1 e^{(-\delta t)}$ to the envelope of the time history of the separation surface displacement. However, because of the energy transfer and beating effect associated with the wave rotation, the logarithmic decrement Δ changes continuously during the initial dozens of free oscillation periods. Therefore, here, the logarithmic decrement Δ is defined as $\Delta = \ln(\xi_1/\xi_l)$, where ξ_l is the peak amplitude of the last free oscillation cycle at P2. It is illustrated that the initial oscillation amplitude has a small effect on the damping rate δ of the separation surface wave, and the damping rate of the present two-layer liquid system is close to 0.05. For Cases A, B, C, and D, the decay of the rotary wave is described well using the exponential formula $\xi = \xi_1 e^{(-\delta t)}$ after

approximately 25, 30, 35, and 45 periods, respectively. Furthermore, the asymmetry of the free oscillation amplitude indicates that the separation surface wave has a higher wave crest and a shallow wave trough, leading to unequal positive and negative displacements and hence different damping rates at large excitation amplitudes.

In our free damping tests, the motions of the separation surface wave were dominated by the first asymmetric mode ($m = n = 1$) of the system. Figure 4 shows the theoretical solution for the wall damping rate δ_{11}^{BL}, the interface damping rate δ_{11}^{IL}, the interior damping rate δ_{11}^{Int}, and the total damping rate δ_{11} at different h_1/H calculated using Equations (7)−(10) for the first asymmetric mode. The experimental damping rates at $h_1/H = 0.5$ are also presented.

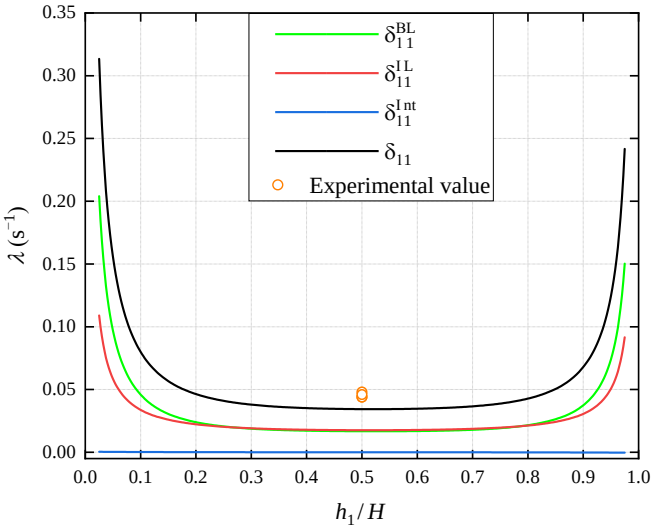

Figure 4. The dependence of the wall damping rate δ_{11}^{BL}, the interface damping rate δ_{11}^{IL}, the interior damping rate δ_{11}^{Int}, and the total damping rate δ_{11} on h_1/H, keeping $H = h_1 + h_2 = 48$ cm for the first asymmetric mode. The experimental damping rates are compared with the theoretical value at $h_1/H = 0.5$.

The interior damping rate δ_{11}^{Int} is negligibly small for liquids with densities of the same order. However, the contribution of δ_{11}^{Int} cannot be ignored anymore when the density of the upper layer is very small, e.g., $\rho_2 \to 0$. In addition, the comparisons between the experimental and theoretical results demonstrate that the theoretical prediction is in good agreement with the experimental measurements, although the theoretical method seems to slightly underestimate the experimental damping rates. This difference is not surprising because Equations (7)−(10) only consider the effect of the linear boundary layer and do not account for various nonlinear effects such as large-amplitude wave rotation, turbulent energy dissipation, and the generation and breaking of short waves. Therefore, Equations (7)−(10) inevitably give smaller viscous damping values than the actual value. Similar differences were observed in studies of 2D free surface sloshing in a rectangular tank [28] and 3D free surface sloshing in a square-base or cylindrical tank [11].

As discussed in Section 2, the lowest natural frequency of the separation surface sloshing can be calculated theoretically using linear potential theory (i.e., Equation (3)) to be $f_1 = 0.434$ Hz. Here, we experimentally verify this theoretical value using the same free damping tests that were also used to determine the viscous damping rate δ. After turning off the forcing, the interface oscillates at its natural frequency. Figure 5a–d show the PSD of the decay of the separation surface displacement at P1 and P2 for Cases A, B, C, and D, respectively. As shown in Figure 5a, the dominant contribution to the decaying separation surface wave comes from the lowest natural frequency f_1, and the theoretical value of the natural frequency is in good agreement with the experimental measurement. However, with an increase in the initial oscillation amplitude, the frequency corresponding

to the dominant spectral peak gradually deviates from the lowest natural frequency f_1. Meanwhile, for Cases B, C, and D, there is a slightly lower spectral peak near the dominant peak in the power spectrum at both P1 and P2. Specifically, the secondary spectral peaks at P1 and P2 correspond to $0.96f_1$ and $0.95f_1$, respectively. Because of the interaction between the contributions from two different frequency components, beating behaviors take place in the decaying separation surface wave in Figure 3c,d. The theoretical study of Miles [29] found that one effect of 3D free surface rotation is the lowest natural frequencies of the 2D planar wave being split. A recent experimental study conducted by Tsarau et al. [30] confirmed the appearance of frequency pairs near the lowest natural frequency in the cylindrical tank with a rotary free liquid surface. This paper further reveals that the rotation of the 3D separation surface wave splits the lowest natural frequency of the system into two neighboring frequencies.

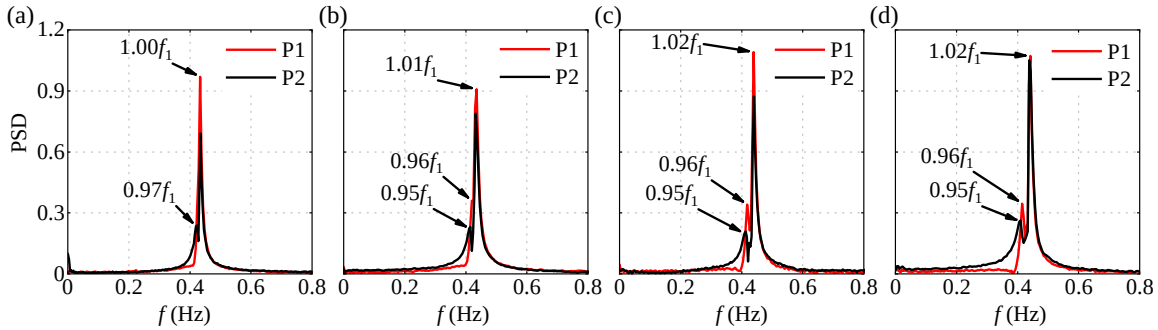

Figure 5. The frequency spectrum of the decaying oscillation at P1 and P2 for (**a**) Case A, (**b**) Case B, (**c**) Case C, and (**d**) Case D. The PSD stems from the time series of the decaying separation surface displacement shown in Figure 3.

4. Amplitude–Frequency Response

In this section, to explore the effects of the excitation frequency on the separation surface sloshing dynamics, the non-dimensional amplitude A/D = 0.05 and a series of non-dimensional frequencies ($0.5 \leq f_e/f_1 \leq 3.0$) are considered. Figure 6 presents the maximum amplitude η_{max} of the separation surface wave response at P1 and P2, made non-dimensional by D, as a function of f_e/f_1. The empty and filled symbols represent the 2D planar motions and 3D rotary motions, respectively. For comparison, the theoretical predictions of the wave response at P1 obtained using Equation (6) are also shown.

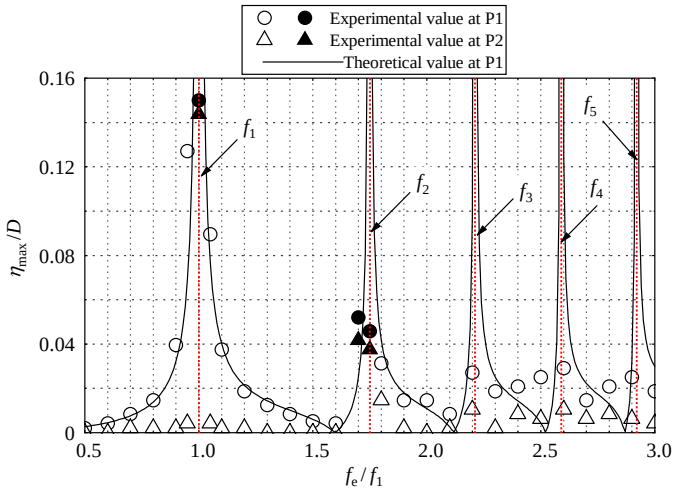

Figure 6. The influence of the excitation frequency f_e/f_1 on the maximum separation surface displacement η_{max}/D at P1 and P2 for the excitation amplitude A/D = 0.05. Empty symbols denote planar waves and filled symbols mark rotary waves.

When starting at $f_e/f_1 = 0.5$ and then increasing f_e/f_1 by small frequency increments, the amplitude of the separation surface wave increases until a critical frequency (i.e., the lowest natural frequency f_1) is reached, at which point the wave form changes to a rotary wave. The occurrence of wave rotation can be clearly depended on not only through visual observation of the video but also through a sudden enlargement of the separation surface wave amplitude at position P2. Interestingly, for $f_e/f_1 = 0.95$, the wave amplitude at P2 is far lower than that at P1, but for $f_e/f_1 = 1.0$, the wave amplitude at P2 is approximately equal to that at P1. When f_e/f_1 is further increased, the wave form changes from rotary to planar, and the amplitude of the sloshing wave rapidly decreases. When f_e is increased further to $f_e = 1.7f_1 = 0.97f_2$, wave rotation occurs again. However, the amplitude of the rotary wave in the second natural mode is significantly smaller than that in the first natural mode. Furthermore, it can be seen that the wave amplitudes in the third, fourth, and fifth natural modes are relatively small; therefore, this paper will focus on the wave response under the first and second natural modes of the system. Furthermore, it is interesting to note that the theoretical solutions for the separation surface wave amplitudes at P1 from linear theory are in good agreement with the experiments when f_e is slightly away from f_1. However, there is a great difference between the theoretical and experimental results when f_e is very close to f_1 or when f_e is in the vicinity of f_2, f_3, f_4, or f_5. First, linear theory gives typical resonance curves with infinite wave amplitudes, as the separation surface wave motion is undamped due to the inviscid assumption of potential flow, and second, the rotary wave regimes under the first and second modes are not captured. Consequently, linear potential theory could only be used to estimate the 2D first-mode planar wave motion in a cylindrical tank.

5. First-Mode Resonance

In this section, the 3D separation surface sloshing dynamics of the lowest natural mode in the completely filled cylindrical tank are systematically explored. First, in order to test the robustness of the rotary wave, we explore the transformation from a planar long wave into a rotary long–short wave regime at the lowest natural frequency by gradually increasing the excitation amplitude. Figure 7 gives the wave response η_{max}/D at P1 and P2 versus A/D ($0.005 \leq A/D \leq 0.1$).

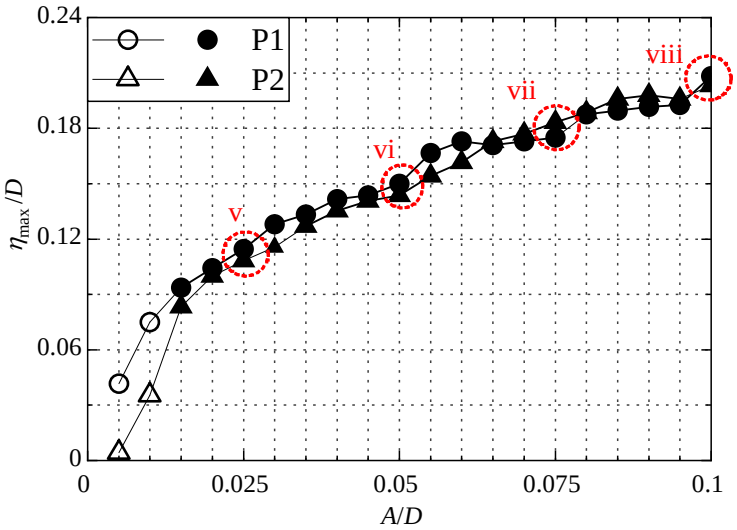

Figure 7. The transformation diagram from the planar long wave regime into the rotary long–short wave regime with increasing amplitude A/D at $f_e/f_1 = 1.0$. v–viii denote case number.

Initially, the movement of the separation surface wave is a planar long wave for $A/D = 0.005$. The wave amplitude at P1 is much larger than that at P2. Then, as A/D is increased to 0.015, the long wave becomes rotary around the axis of the tank. As a result,

the wave amplitude at P2 is very close to that at P1. When A/D is equal to 0.02, short waves are generated at the interface, and thus the rotary long wave changes into a rotary long–short wave. With a further increase in A/D, the amplitude of the rotary wave is increased accordingly, but there is no change in the wave mode. The above findings clearly illustrate that when the rotary wave of the primary natural mode is built, it is very robust due to its persistence with a continuous increase in the driving energy.

To further study the rotary sloshing dynamics of the primary natural mode, four experimental cases (Case v: A/D = 0.025, Case vi: A/D = 0.05, Case vii: A/D = 0.075, and Case viii: A/D = 0.1) marked in Figure 7 are considered here. Figure 8 presents the time series of the separation surface displacement at P1 and P2 for the four increasing excitation amplitudes. In all cases, it is clearly seen that beating-like behavior takes place at the interface in the initial dozens of oscillation cycles, but eventually, the movement of the separation surface wave attains a steady state with a fixed sloshing amplitude. In general, the larger the excitation amplitude, the shorter the period of the initial unsteady state. Furthermore, the steady-state wave amplitudes at P1 are smaller than those at P2, which demonstrates that the strong nonlinearity caused by the first-mode resonance transfers energy in the direction perpendicular to that of the tank's movement.

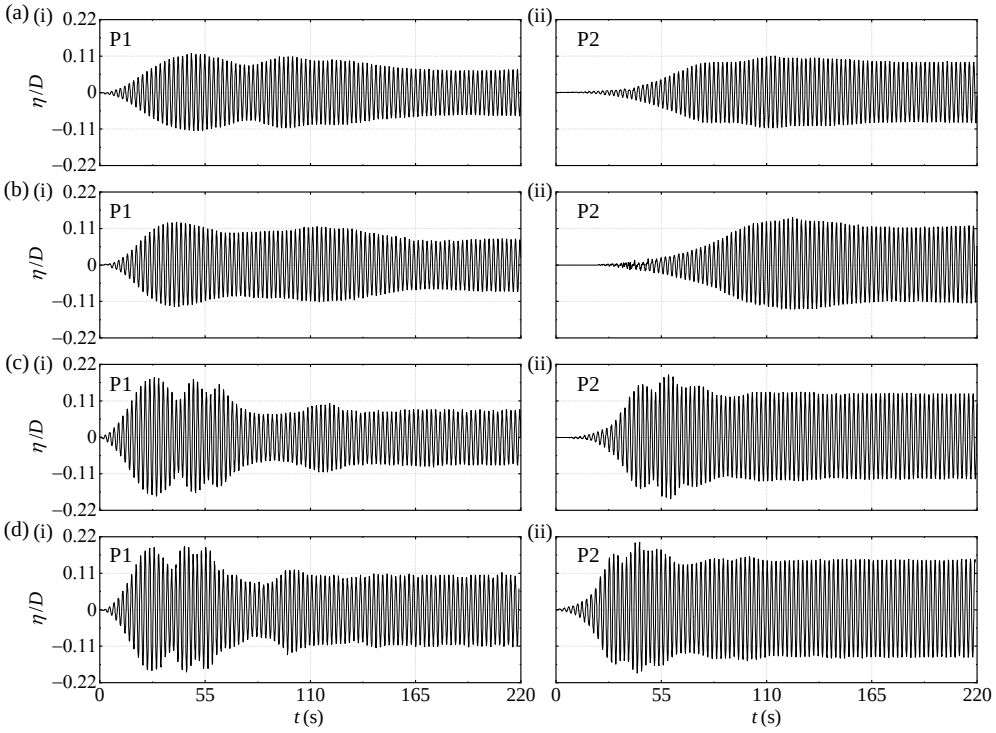

Figure 8. The time series of the separation surface displacement at (**i**) P1 and (**ii**) P2 for increasing excitation amplitudes. (**a**) Case v: A/D = 0.025, (**b**) Case vi: A/D = 0.05, (**c**) Case vii: A/D = 0.075, and (**d**) Case viii: A/D = 0.1.

The strong nonlinearity shown in Figure 8 can be further illuminated by the frequency spectrum analysis in Figure 9. In all the sloshing cases, the main contribution to the wave response is the lowest natural frequency. Furthermore, there is another spectral peak in the frequency near the first-mode natural frequency. The interaction between these two frequencies leads to the appearance of descending and ascending trends in the separation surface displacement.

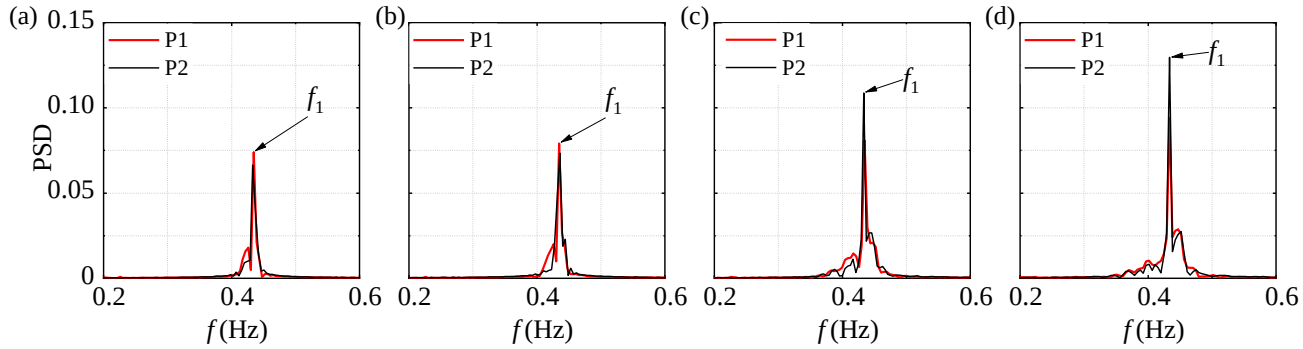

Figure 9. The frequency spectrum of the separation surface displacement at P1 and P2 for increasing excitation amplitudes. (**a**) Case v: A/D = 0.025, (**b**) Case vi: A/D = 0.05, (**c**) Case vii: A/D = 0.075, and (**d**) Case viii: A/D = 0.1.

Figure 10 shows a parametric curve of the separation surface displacement during 0–110 s and 110–220 s at P1 and P2 for Cases v, vi, vii, and viii. It further shows the effect of the excitation amplitude on the nonlinear oscillation at the initial stage of the separation surface rotary wave.

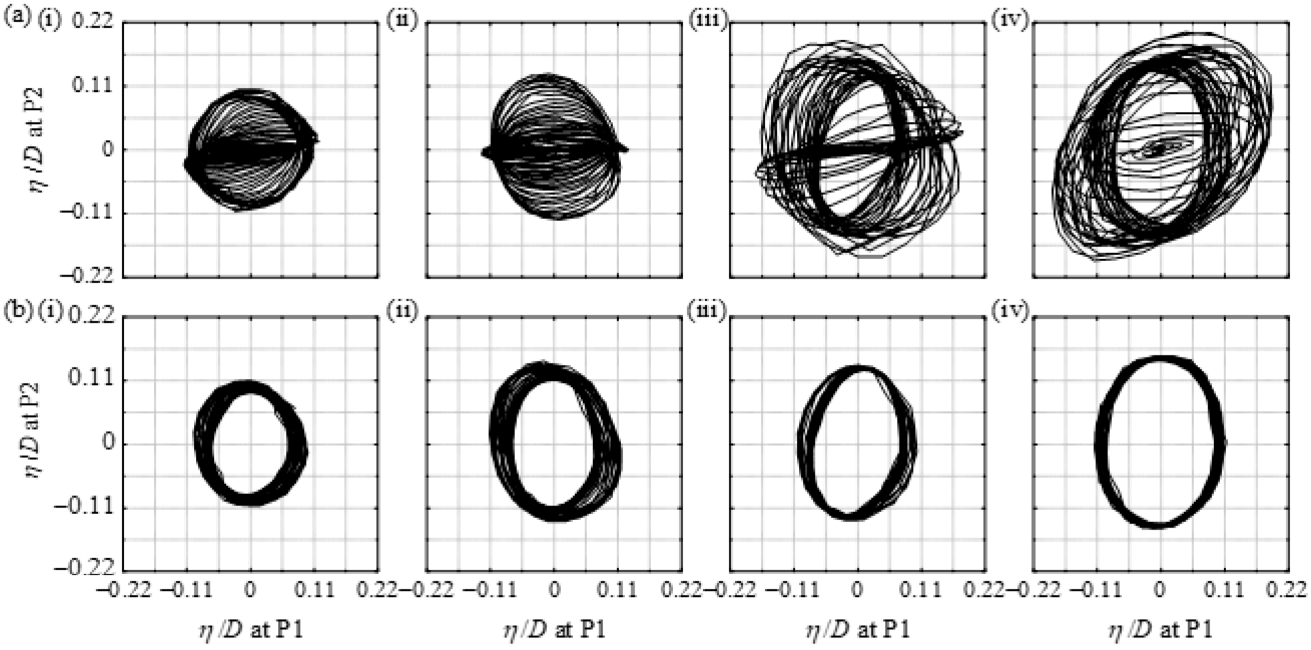

Figure 10. The parametric curve of the separation surface displacement during (**a**) 0–110 s and (**b**) 110–220 s at P1 and P2 for increasing excitation amplitudes. (**i**) Case v: A/D = 0.025, (**ii**) Case vi: A/D = 0.05, (**iii**) Case vii: A/D = 0.075, and (**iv**) Case viii: A/D = 0.1.

Figure 11 shows separation surface wave images at five typical time instants in the primary natural mode for Cases v, vi, vii, and viii. All the pictures were extracted from the steady state of the rotary motion, as seen in Figure 8. It is clearly seen that the strength of the short waves, including the amplitude and quantity, increases with an increase in the excitation amplitude. Furthermore, the rotation direction in all cases is anticlockwise, which further suggests the robustness of the separation surface rotary wave.

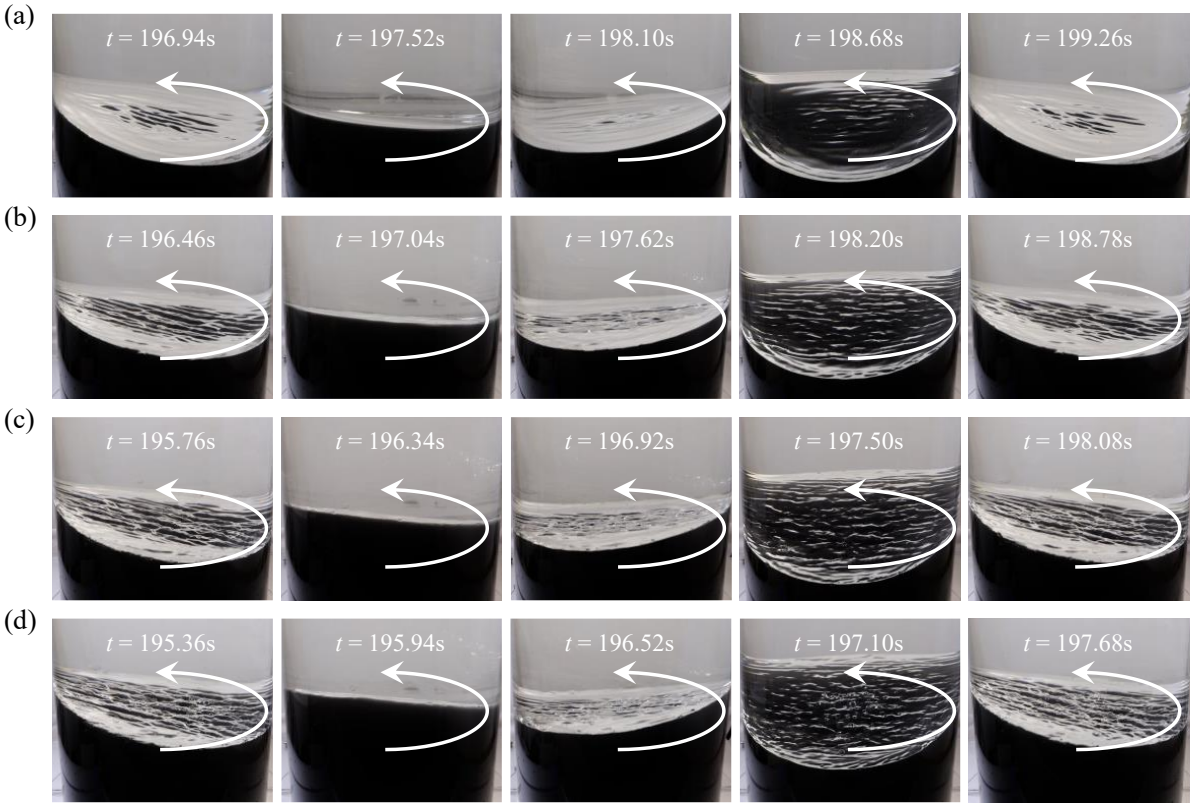

Figure 11. The evolution of the wave form viewed perpendicular to the direction of tank movement for increasing excitation amplitudes. (**a**) Case v: $A/D = 0.025$, (**b**) Case vi: $A/D = 0.05$, (**c**) Case vii: $A/D = 0.075$, and (**d**) Case viii: $A/D = 0.1$.

6. Second-Mode Resonance

In this section, the 3D separation surface sloshing dynamics of the second natural mode in the completely filled cylindrical tank are investigated. To begin with, in order to illustrate the evolutions of the second-mode wave regime, Figure 12 shows the sloshing wave amplitude responses $\eta_{\max}/D$ at P1 and P2 for $f_e/f_2 = 1.0$ as a function of the excitation amplitudes A/D ($0.005 \leq A/D \leq 0.1$). It can be seen that there are three types of second-mode wave regimes: the second-mode standing long wave, the second-mode rotary long wave, and the second-mode rotary long–short wave regimes. When A/D is less than the critical amplitude, which is 0.02, the amplitude of the separation surface wave at P2 is almost always zero, which means that the wave regime is a second-mode standing wave. When A/D is increased to 0.025, the strong nonlinearity of the system transfers energy in the perpendicular direction to the tank's movement, leading to the appearance of rotation of the wave crest and wave trough. The edge of the wave has to follow the movement of the internal wave crest, and thus the wave amplitude at P2 is not zero. With an increasing A/D, an abrupt increase in the wave amplitude at P2 takes place, owing to the large-amplitude rotary motion of the edge of the wave caused by the strong nonlinear effect. When A/D is further increased to 0.045, multitudinous short waves appear in the separation surface wave, and thus the wave regime changes into a second-mode rotary long–short wave. Similar to the first-mode rotary long–short wave, the second-mode rotary long–short wave is very robust because of its persistence with a continuous increase in A/D. In addition, it should be noted that when the excitation frequency approach the second-mode natural frequency, the rotary motion is a steady-state motion that rotates around the tank wall.

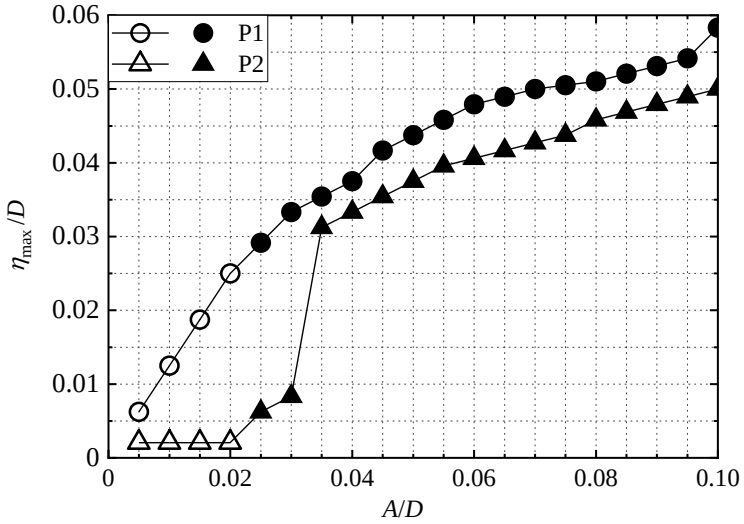

Figure 12. The transition diagram from the second-mode standing long wave regime to the second-mode rotary long–short wave regime with increasing amplitude A/D and the excitation frequency kept fixed at $f_e/f_2 = 1.0$. Empty symbols indicate non-rotary waves, and filled symbols represent rotary waves.

Figure 13 plots the (a, c) time series, (b) frequency spectrum, and (d) parametric curve of the separation surface displacement at P1 and P2 for $f_e/f_2 = 1.0$ and $A/D = 0.1$. Obviously, typical resonance behavior occurs at both P1 and P2 at the interface, as seen in Figure 13a,c. The frequency spectrum in Figure 13b indicates that only the second-mode natural frequency makes contributions to the forced response. Furthermore, similar to the parametric curve of the first-mode resonant sloshing in Figure 10, Figure 13d illustrates that the motion of the separation surface wave is a stable rotary wave.

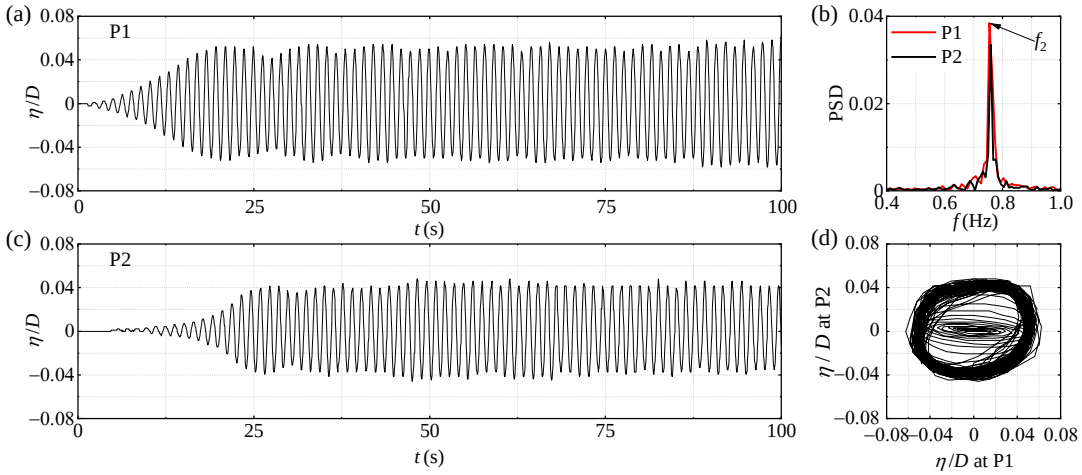

Figure 13. The (**a**,**c**) time series, (**b**) frequency spectrum, and (**d**) parametric curve of the separation surface displacement at P1 and P2 for $f_e/f_2 = 1.0$ and $A/D = 0.1$.

Figure 14 shows the evolution of the separation surface wave at the second natural frequency and for $A/D = 0.1$. The second-mode resonant sloshing dynamics can be represented in three stages: the second-mode standing long wave, second-mode standing long–short wave, and second-mode rotary long–short wave stages. During the first few movement cycles, the wave form is a second-mode standing long wave with a wavelength $\lambda = 2D/3$. Its profile is similar to that of 2D free surface and separation surface waves in a rectangular tank [23]. Meanwhile, the minima of the wave troughs and the maxima of the wave crests always lie on the axis of the tank's movement, as seen in Figure 14a,b. Subse-

quently, a large number of short waves are produced at the separation interface, and the wave form transforms into a second-mode standing long–short wave, as seen in Figure 14c. Finally, the nonlinear effect makes the crest of the standing wave deviate from the axis of the tank's movement and rotate around the tank in the anticlockwise direction, as seen in Figure 14d,e. It is worth noting that the line connecting the minima of the wave troughs and the maxima of the wave crests is perpendicular to the tank's movement direction at t = 24.80, 25.44, 26.08, 35.36, 36.00, and 36.64 s.

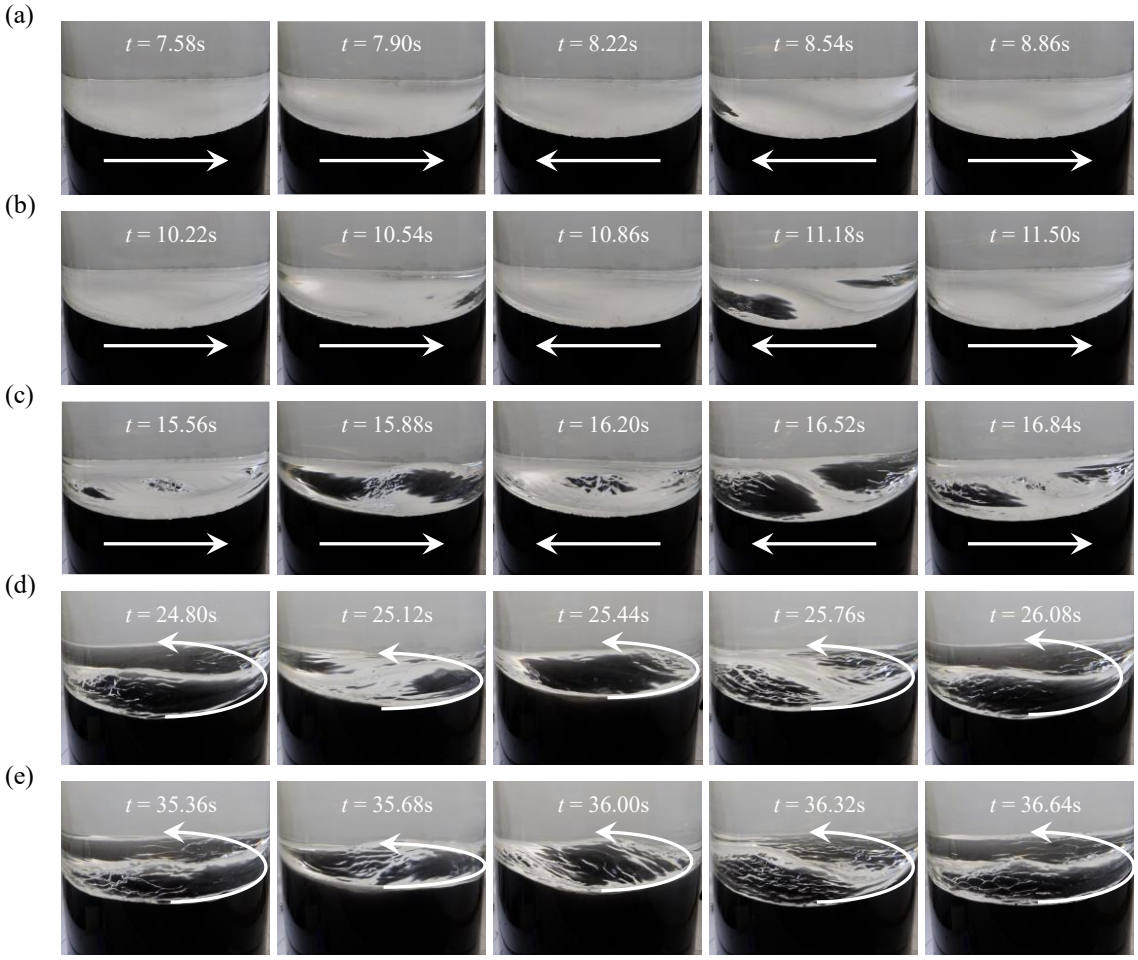

Figure 14. The evolution of the wave form viewed perpendicular to the direction of tank movement at f_e/f_2 = 1.0 and for A/D = 0.1. Panels (**a**–**e**) denote five different oscillation period.

7. Conclusions

In this paper, to elucidate the 3D resonant sloshing dynamics of an oil–water interface in an offshore cylindrical wet storage tank, hundreds of experimental cases were conducted in a completely filled cylindrical tank with two liquids—dyed water and mineral oil. The model tank was installed on a shake table and promoted using sinusoidal horizontal motion. Twenty non-dimensional excitation amplitudes, i.e., A/D = 0.005−0.1, with small increments of 0.005, were tested to examine the effects of the excitation amplitude on the separation surface sloshing dynamic. Meanwhile, dozens of non-dimensional excitation frequencies f_e/f_1, ranging from 0.5 to 3.0 and including the natural frequencies of the first, second, third, fourth, and fifth modes, were employed to examine the effect of the excitation frequency on the separation surface sloshing dynamics. To the best of the authors' knowledge, this is the first time that 3D separation surface sloshing dynamics have been systematically studied in a completely filled cylindrical tank. Some interesting findings were uncovered.

The free damping test can be used to determine the viscous damping rate of the system and verify the theoretical results of the lowest natural sloshing frequency. In decay experiments, the movement of the separation surface wave is a rotary wave with a fixed amplitude before the cessation of the tank's movement, but it fades into a rotary wave with a decreasing amplitude after the driving is stopped. Note that beating behavior occurs at the interface during the decaying state. The frequency spectrum shows there are two dominant frequencies close to the lowest natural frequency, which reveals that the rotation of the separation surface wave splits the lowest natural frequency of the planar wave into two neighboring frequencies. Because of the coupling between the contributions from two different frequency components, beating behaviors take place in the decaying separation surface wave. Similar discoveries were made in a theoretical study and an experimental study on free surface rotary sloshing in a cylindrical tank.

When horizontal harmonic excitation is exerted on the tank, the separation interface does not inevitably respond with 2D steady-state motion, where it oscillates in the direction of the tank's movement. Rather, an intricate 3D wave may be generated at the interface that rotates around the wall. The present study found that the separation surface wave response depends strongly on the excitation frequency, and the maximum effect occurs when the excitation frequency matches the natural frequencies of the system. The wave rotation occurs not only at the lowest natural frequency but also at the second-mode natural frequency. However, the amplitude of the rotary wave at the second-mode natural frequency is significantly smaller than that at the lowest natural frequency. Moreover, the experiments suggested that the wave amplitudes at the third, fourth, and fifth natural frequencies are relatively small, similar to 2D free surface or separation surface sloshing in a rectangular tank. Therefore, this paper focuses on the first- and second-mode natural frequency of the system.

When the excitation frequency is equal to the first-mode natural frequency of the system, there are three types of separation surface wave regimes: planar long wave, nonplanar long–short wave, and rotary long–short wave regimes. The planar long wave is a 2D stable motion with a fixed wave amplitude at the wall. The nonplanar long–short wave is a 3D harmonic motion with a fixed wave amplitude at the wall, and it is not 2D as a result of the generation of multitudinous short waves at the interface. With a further increase in the excitation amplitude, the amplitude of the rotary wave and the strength of the short waves, including the amplitude and quantity, are increased accordingly, but there is no change in the wave mode.

When the excitation frequency is equal to the second-mode natural frequency of the system, there are three types of second-mode wave regimes: the second-mode standing long wave, second-mode rotary long wave, and second-mode rotary long–short wave regimes. For the second-mode rotary long–short wave regime, during the first few oscillation cycles, the wave form is that of a second-mode standing long wave with a wavelength $\lambda = 2D/3$, and its profile is similar to the 2D free surface and separation surface waves in a rectangular tank. Meanwhile, the minima of the wave troughs and the maxima of the wave crests always lie on the axis of the tank's movement. Subsequently, a large number of short waves are produced at the interface, and thus the wave form transforms into a second-mode standing long–short wave. Finally, the nonlinear effect makes the crest of the standing wave deviate from the axis of the tank's movement and rotate around the tank in the anticlockwise direction.

This work has demonstrated that the 3D separation surface sloshing dynamics in a two-layer liquid system are much more intricate than the 3D free surface sloshing dynamics in a single-layer liquid system due to the generation of multitudinous short waves at the interface.

Author Contributions: Conceptualization, D.L.; Methodology, D.L. and Y.C.; Formal analysis, D.L. and X.W.; Investigation, X.W. and Y.C.; Writing—original draft, D.L. and X.W.; Writing—review & editing, D.L. and Y.C.; Supervision, Y.C. All authors have read and agreed to the published version of the manuscript.

Funding: This study was supported by the National Natural Science Foundation of China (Grant No. 51809163).

Institutional Review Board Statement: Not applicable.

Informed Consent Statement: Not applicable.

Data Availability Statement: Data is contained within the article.

Conflicts of Interest: The authors declare no conflict of interest.

References

1. Liu, D.; Lei, L.; Wang, J.; Han, P.; You, Y.; Liu, W.; Wang, C.; Chen, G.; Shi, Y. Study on oil content in discharged water from oil-water replacement storage offloading system of deepwater SDPSO platform. *China Offshore Oil Gas* **2021**, *33*, 164–171.
2. Wang, W.; Wang, L.; Du, Y.; Huang, Y. Novel controller for the coupled surge-pitch problem by controlling the metacentric height of sandglass-type FDPSO. *Ocean Eng.* **2022**, *251*, 111095. [CrossRef]
3. Halkyard, J.; Choi, G.; Prislin, I.; Steen, A.; Hawley, P. The floating drilling, production, storage, and offloading vessel for the large deepwater field development. *Int. J. Ocean Eng. Technol.* **2000**, *3*, 1–7.
4. Wheaton, S.; Clark, S.; Cruickshank, P. The Solan field subsea oil storage tank after one year's operation west of Shetland, UK-is it a concept that has delivered. In Proceedings of the SPE Offshore Europe Conference & Exhibition, Aberdeen, UK, 5–8 September 2017; SPE-186161.
5. Widianto, W.; Khalifa, J.; Younan, A.; Karlsson, T.; Stuckey, P.; Gjorven, A. Design of Hebron gravity based structure for iceberg impact. In Proceedings of the Twenty-third International Offshore and Polar Engineering, Anchorage, AK, USA, 30 June–5 July 2013; pp. 1127–1134.
6. Faltinsen, O.M.; Timokha, A.N. *Sloshing*; Cambridge University Press: Cambridge, UK, 2009.
7. Ibrahim, R. Recent advances in physics of fluid parametric sloshing and related problems. *J. Fluids Eng.* **2015**, *137*, 090801. [CrossRef]
8. Zheng, J.; Xue, M.; Dou, P.; He, Y. A review on liquid sloshing hydrodynamics. *J. Hydrodyn.* **2021**, *33*, 1089–1104. [CrossRef]
9. Shen, Y.; Firoozkoohi, R.; Greco, M.; Faltinsen, O.M. Experimental investigation of a closed vertical cylinder-shaped fish cage in waves. *Ocean Eng.* **2021**, *236*, 109444. [CrossRef]
10. Ikeda, T.; Ibrahim, R.A.; Harata, Y.; Kuriyama, T. Nonlinear liquid sloshing in a square tank subjected to obliquely horizontal excitation. *J. Fluid Mech.* **2012**, *700*, 304–328. [CrossRef]
11. Faltinsen, O.M.; Timokha, A.N. Resonant three-dimensional nonlinear sloshing in a square-base basin. Part 4. Oblique forcing and linear viscous damping. *J. Fluid Mech.* **2017**, *822*, 139–169. [CrossRef]
12. Tao, Y.; Zhu, R.; Gu, J.; Wei, Q.; Hu, F.; Xu, X.; Zhang, Z.; Li, Z. Sloshing response of an aquaculture vessel: An experimental study. *J. Mar. Sci. Eng.* **2023**, *11*, 2122. [CrossRef]
13. Ibrahim, R. *Liquid Sloshing Dynamics: Theory and Applications*; Cambridge University Press: Cambridge, UK, 2005.
14. Igbadumhe, J.; Furth, M. Hydrodynamic analysis techniques for coupled seakeeping-sloshing in zero speed vessels: A review. *J. Offshore Mech. Arct. Eng.* **2021**, *143*, 020801. [CrossRef]
15. Liu, D.; Cai, W.; Lu, T. Comparative assessment of liquid sloshing in dry and wet storage tank of floating offshore platform. *Mar. Struct.* **2023**, *90*, 103425. [CrossRef]
16. Liu, D.; Li, Y. Primary and secondary resonance phenomenon for two-layer liquid sloshing in a rectangular container under horizontal excitation. *Phys. Fluids* **2024**, *36*, 032103. [CrossRef]
17. Xue, M.; Cao, Z.; Yuan, X.; Zheng, J.; Lin, P. A two-dimensional semi-analytic solution on two-layered liquid sloshing in a rectangular tank with a horizontal elastic baffle. *Phys. Fluids* **2023**, *35*, 062116.
18. Cao, W.; Li, X.; Gao, Y.; Li, X.; Liu, Z. A numerical analysis of sloshing dynamics of two-layer liquid with a free surface. *Ocean Eng.* **2023**, *268*, 113295. [CrossRef]
19. Frankiewicz, T.; Lee, C. Using computational fluid dynamics (CFD) simulation to model fluid motion in process vessels on fixed and floating platforms. In Proceedings of the SPE Annual Technical Conference and Exhibition, San Antonio, TX, USA, 29 September–2 October 2002.
20. Lu, Y.; Chai, S. CFD verification of engineering options for mitigating liquid sloshing in topside vessels on a floating production facility. In Proceedings of the SPE Annual Technical Conference and Exhibition, Denver, CO, USA, 21–24 September 2008.
21. Cen, K.; Song, B.; Li, C.; Jia, M. Liquid sloshing suppression for three-phase separators installed on floating production unit. *J. Offshore Mech. Arct. Eng.* **2018**, *140*, 041403. [CrossRef]
22. Luo, M.; Su, X.; Lin, P.; Khayyer, A.; Zhao, X. Investigation of two-layer liquid sloshing by using the consistent particle method. *Int. J. Offshore Polar Eng.* **2022**, *32*, 7–15. [CrossRef]
23. Horstmann, G.; Herreman, W.; Weier, T. Linear damped interfacial wave theory for an orbitally shaken upright circular cylinder. *J. Fluid Mech.* **2020**, *891*, A22. [CrossRef]
24. Horstmann, G.; Wylega, M.; Weier, T. Measurement of interfacial wave dynamics in orbitally shaken cylindrical containers using ultrasound pulse-echo techniques. *Exp. Fluids* **2019**, *60*, 56. [CrossRef]

25. Reclari, M.; Dreyer, M.; Tissot, S.; Obreschkow, D.; Wurm, F.M.; Farhat, M. Surface wave dynamics in orbital shaken cylindrical containers. *Phys. Fluids* **2014**, *26*, 052104. [CrossRef]
26. Dodge, F. *The New "Dynamic Behavior of Liquids in Moving Containers"*; NASA SP-106; Southwest Research Institute: San Antonio, TX, USA, 2000.
27. Simonini, A.; Fontanarosa, D.; De Giorgi, M.G.; Vetrano, M.R. Mode characterization and damping measurement of liquid sloshing in cylindrical containers by means of Reference Image Topography. *Exp. Therm. Fluid Sci.* **2021**, *120*, 110232. [CrossRef]
28. Bäuerlein, B.; Avila, K. Phase lag predicts nonlinear response maxima in liquid-sloshing experiments. *J. Fluid Mech.* **2021**, *925*, A22. [CrossRef]
29. Miles, J.W. Internally resonant surface waves in circular cylinder. *J. Fluid Mech.* **1984**, *149*, 1–14. [CrossRef]
30. Tsarau, A.; Lugni, C.; Lucarelli, A.; Kristiansen, D.; Lader, P. Sloshing in a rotating liquid inside a closed sea cage for fish farming. *Phys. Fluids* **2021**, *33*, 037114. [CrossRef]

Disclaimer/Publisher's Note: The statements, opinions and data contained in all publications are solely those of the individual author(s) and contributor(s) and not of MDPI and/or the editor(s). MDPI and/or the editor(s) disclaim responsibility for any injury to people or property resulting from any ideas, methods, instructions or products referred to in the content.